

Short Communication

## Mitigating Particle Cracking and Surface Deterioration for Better Cycle Stability by Encapsulating NCM811 primary particles into LiBO<sub>2</sub>

Cheng Yang<sup>1</sup>, Liangjun Zhou<sup>2,\*</sup>, Wang Hu<sup>2</sup>, Weifeng Wei<sup>2</sup>

<sup>1</sup> School of Metallurgy and Environment, Central South University, Changsha 410083, P.R. China

<sup>2</sup> State Key Laboratory of Powder Metallurgy, Central South University, Changsha, Hunan, 410083, P. R. China

\*E-mail: [alexander-zhou@csu.edu.cn](mailto:alexander-zhou@csu.edu.cn)

Received: 29 August 2020 / Accepted: 11 November 2020 / Published: 30 November 2020

Nickel-rich layered cathode materials have drawn a lot of attention due to their much higher energy density and lower cost. However, there is still a challenge in long-term cycling stability for practical application. In this work, a modification strategy of encapsulation on primary particles of NCM811 is applied to improve the electrochemical performance of LiNi<sub>0.80</sub>Co<sub>0.10</sub>Mn<sub>0.10</sub>O<sub>2</sub> (NCM811) by effectively mitigating particle cracking and surface deterioration of NCM811. Compared with the general NCM811 (G0-811), the optimized NCM811 (O3-811) exhibits higher specific capacity and much improved cycle stability. After 800 cycles, the capacity retention of O3-811 is 91.8%, while the capacity of G0-811 fades rapidly in 430 cycles. Cross section SEM, EIS and DSC have been applied for further observation on the cycled O3-811 in comparison with G0-811. The results confirm that the encapsulating NCM811 primary particles as well as secondary spheres into LiBO<sub>2</sub> successfully improves the electrochemical performances and structure stability of NCM811, which is hopeful for commercial application.

**Keywords:** Ni-rich cathode materials, particle cracking, surface deterioration, cycle stability

### 1. INTRODUCTION

With the rapid development of plug-in hybrid electric vehicles (PHEVs), electric vehicles (EVs), and back-up power devices, the demand for high energy density lithium-ion batteries (LIBs) is growing fast. Among all the cathode material candidates, Ni-rich layered cathode materials, represented as a formula of LiNi<sub>x</sub>M<sub>1-x</sub>O<sub>2</sub> (M = Co, Mn, Al, W, etc. x≥0.6), are now drawing more and more attentions due to their higher capacity, slighter toxicity and lower cost.[1-3] Unfortunately, there are commonly

realized problems hindering  $\text{LiNi}_x\text{M}_{1-x}\text{O}_2$  from practical usage: 1) severe surface deterioration, introduced by the high reactivity between cathode and electrolyte, leading to deactivation phase transformation growth from the surface to the bulk; [4, 5] 2) disconnection between the  $\text{LiNi}_x\text{M}_{1-x}\text{O}_2$  primary particles, as well as between the active materials and current collectors, which is ascribed to gas release and the change of cell volume during the lithium intercalation and deintercalation, resulting in serious capacity fading and polarization increasing. [3, 5, 6-9]

Extensive efforts have previously shown that surface coating layer such as ceramic oxides, phosphates, and fluorides, can prevent electrode materials from the electrolyte corrosion by acting as barriers, thus leading to better cycle performance. [10-14] Most of those surface strategies either managing to uniformly disperse coating additives on secondary particles or fabricating a complex outlayer. However, there are hardly any studies about surface modification on strengthening the intergranular contact between primary particles. [15, 16]

Herein, an optimized surface modification method, encapsulating the primary particles as well as secondary spheres of Ni-rich cathode material ( $\text{LiNi}_{0.8}\text{Co}_{0.1}\text{Mn}_{0.1}\text{O}_2$ , NCM811) into lithium boron oxides, is introduced to restrain crack growth and disconnection between primary particles. After 800 cycles, the obtained NCM811 exhibits superior electrochemical performance with energy density up to 294 Wh/kg, and better capacity retention (more than 91%) in a pouch type cell. These results make this method a promising approach to promote the commercial usage of Ni-rich cathode materials. [17-19]

## 2. EXPERIMENTAL

### 2.1. Materials Preparation synthesis

$\text{Ni}_{0.8}\text{Co}_{0.1}\text{Mn}_{0.1}(\text{OH})_2$  was synthesized through a hydroxide coprecipitation method. The specific process of  $\text{Ni}_{0.8}\text{Co}_{0.1}\text{Mn}_{0.1}(\text{OH})_2$  preparation was described elsewhere. [20,21] The  $\text{LiNi}_{0.8}\text{Co}_{0.1}\text{Mn}_{0.1}\text{O}_2$  was synthesized by mixing the precursors  $\text{Ni}_{0.8}\text{Co}_{0.1}\text{Mn}_{0.1}(\text{OH})_2$  with  $\text{LiOH}\cdot\text{H}_2\text{O}$  at a molar ratio of 1:1.08 (8% excess of  $\text{LiOH}\cdot\text{H}_2\text{O}$ ). Then, the mixture powder was annealed at 650 °C for 4 h, and then 830 °C for 12 h at 5 °C  $\text{min}^{-1}$  under flowing oxygen. After being washed with water, and post sintering at 650 °C for 6h, the powders were collected and noted as G0-811.

For  $\text{LiBO}_2$  encapsulation on NCM811, G0-811,  $\text{H}_3\text{BO}_3$  and  $\text{LiOH}\cdot\text{H}_2\text{O}$  were used as raw materials. The content of boron was controlled to be 1000, 3000 and 5000 ppm. For the typical process,  $\text{H}_3\text{BO}_3$  was dissolved into a mixture of alcohol and water. The pH of the solution was adjust by  $\text{LiOH}\cdot\text{H}_2\text{O}$  to form a homogenous solution. Then, 5 kg G0-811 were dispersed into the solution and stirred under 65 °C to evaporate the solvent. After being dried and grounded, the mixture was afterwards transferred in a batch-type furnace, and annealed according the following process: 250 °C for 5 h and 500 °C for 5 h at 1.5 °C/min. Finally, thus treated powders were collected and noted as O1-811, O3-811 and O5-811 in accordance to the boron content for each sample.

### 2.2. Materials Characterization

The chemical composition of the as-prepared  $\text{LiNi}_{0.8}\text{Co}_{0.1}\text{Mn}_{0.1}\text{O}_2$  materials were determined using inductively coupled plasma-atomic emission spectrometry (ICP-OES). The morphologies and

crystallographic structures were measured by scanning electron microscopy (SEM, FEG250, FEI QUANTA). The plan-view and cross-sectional view morphology was characterized using field-emission scanning electron microscopy (FESEM, FEG250, FEI QUANTA). The cross-sectional samples analyzed by FESEM and scanning transmission electron microscopy (STEM) were sliced and thinned using traditional lift-out focus ion beam (FIB, FEI Helios Nano Lab G3) process at 2 to 30 kV. X-ray diffraction (XRD, ADVANCE D8, Bruker), and transmission electron microscopy (TEM, JEM-2100F, JEOL).

### 2.3. Electrochemical Testing

During the process of fabricating the working electrodes, a slurry of the active material, polyvinylidene fluoride and conductive agent (SP 1.5%+KS-15 3.5%), at a weight ratio of 92.5:2.5:5 in N-methyl-2-pyrrolidone was pasted onto an Al foil and dried at 110 °C for 6 h in a vacuum oven. Afterwards, the coated foil was punched into circular pieces with a diameter of 12 mm, and the loading active material was around 11 mg. CR2032 coin-type half cells consisting of an as-prepared cathode, a Li metal anode, a Celgard 2325 separator, and 1 M LiPF<sub>6</sub> in EC/EMC/DEC (1:1:1 by weight) electrolyte solution were assembled in an Ar-filled glovebox. Electrochemical tests of the as-assembled coin cells were conducted using a battery testing system (LANHE CT2001A, Wuhan LAND Electronics Co., P. R. China) at 2.8-4.3 V at different current densities. Electrochemical impedance spectroscopy (EIS) was carried out using Princeton PARSTAT 4000 in a frequency range from 100 kHz to 0.01 Hz with an AC amplitude of 5 mV.

For the differential scanning calorimetry (DSC) experiments, the coin cell was charged to 4.3 V after 2 cycles. After the cells are disassembled, the positive electrode was scraped from the aluminum current collector. Approximately 5 mg of the positive electrode with about 2.6 μg electrolyte was hermetically sealed in a stainless steel pan and measurements were conducted at a heating rate of 1 °C·min<sup>-1</sup>.

For further test of G0-811 and O3-811 in pouch cells, thus the obtained NCM811 for electrode were prepared by mixture slurry of carbon black (1.5 wt%), PVDF (1.3 wt%), CNT (0.8 wt%), and NCM811 material (96.4 wt%). An anode material of silicon oxide/graphite composite with specific capacity of 420 mAh/g was used. The capacity balance of anode to cathode was approximately 1.08 for pouch cells. The surface mass density of cathode and anode (SiO<sub>x</sub>/C, 10 wt% SiO<sub>x</sub>) were around 390 g/cm<sup>2</sup> and 180 mg/cm<sup>2</sup>, respectively.

## 3. RESULTS AND DISCUSSION

The schematic illustration of encapsulating NCM811 with boron oxide is displayed in Figure S1, which is carried out by wet dispersion and deposition of boronic acid and lithium hydroxide on the surface of both primary and secondary particles. Since boronic acid melts at around 250 °C, the coating material can further infiltrate into the pores and interspaces of the bulk NMC811. [22] Finally, lithium

boric oxides are obtained with the further transformation reaction along the post heat treatment. The composition of G0-811, O1-811, O3-811 and O5-811 were collected by the ICP-OES, and according to the results given in Table S1, the practical content of boron in O1-811, O3-811 and O5-811 are quite close to the expectation values.

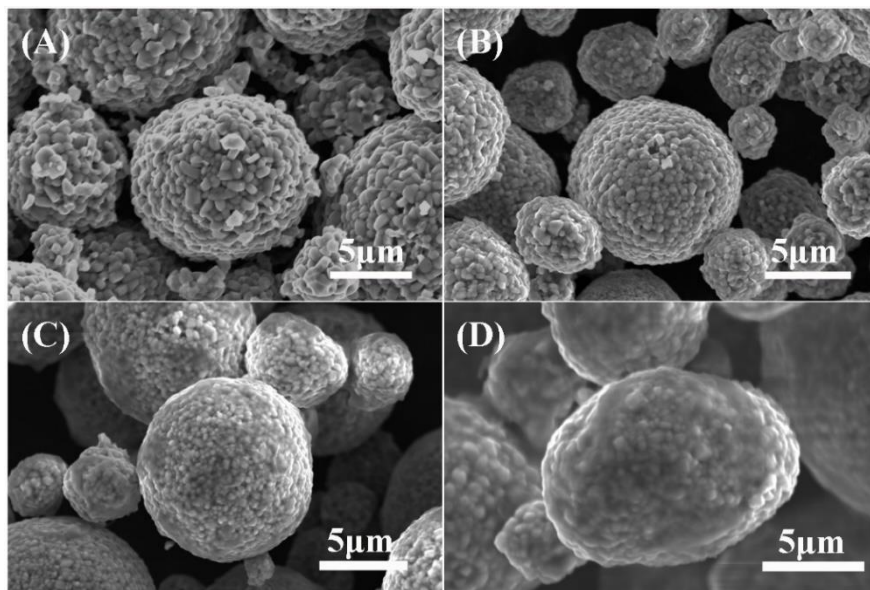


**Figure 1.** SEM images for (A) G0-811, (B) O1-811, (C) O3-811 and (D) O5-811; (E) the XRD patterns for NCM811 samples.

In order to further specify the effectiveness of coating on NCM811, SEM images are given in Figure 1. It can be obviously seen that G0-811 has a bald surface. However, with the increase of boron content, the coating layer becomes dimmer and thicker. Moreover, the particle package becomes less porous after modification, which can be further confirmed in Figure S2.

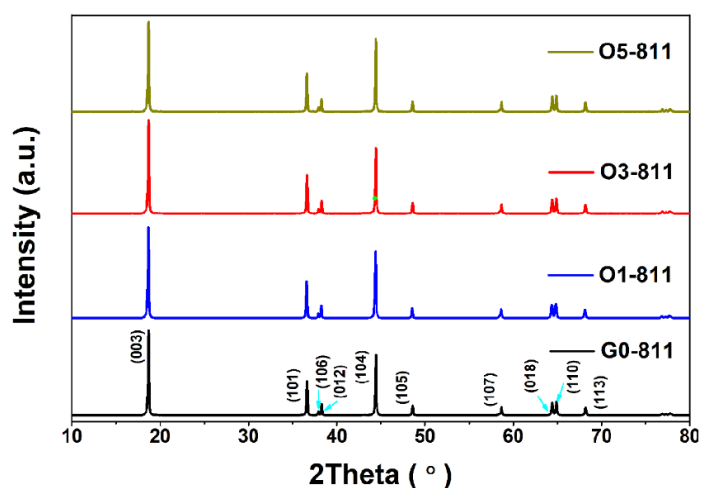


**Figure 2.** the XRD patterns for NCM811 samples.

Powder X-ray diffraction (XRD) is employed for structure characterization of G0-811, O1-811, O3-811 and O5-811. All patterns displayed in Figure 2 (E) can be indexed to a well-defined layer

structure based on a hexagonal  $\text{NaFeO}_2$  structure with an  $R\bar{3}m$  space group. Meanwhile, the splitting of (006)/(102) and (108)/(110) peaks are both observed (see Figure S3), indicating the highly ordered layered structure.[23-24] No extra diffraction peaks are observed after surface modification, which signifies that such post treatment on G0-811 hardly introducing impurity, and the content of boric oxides is at very low level.

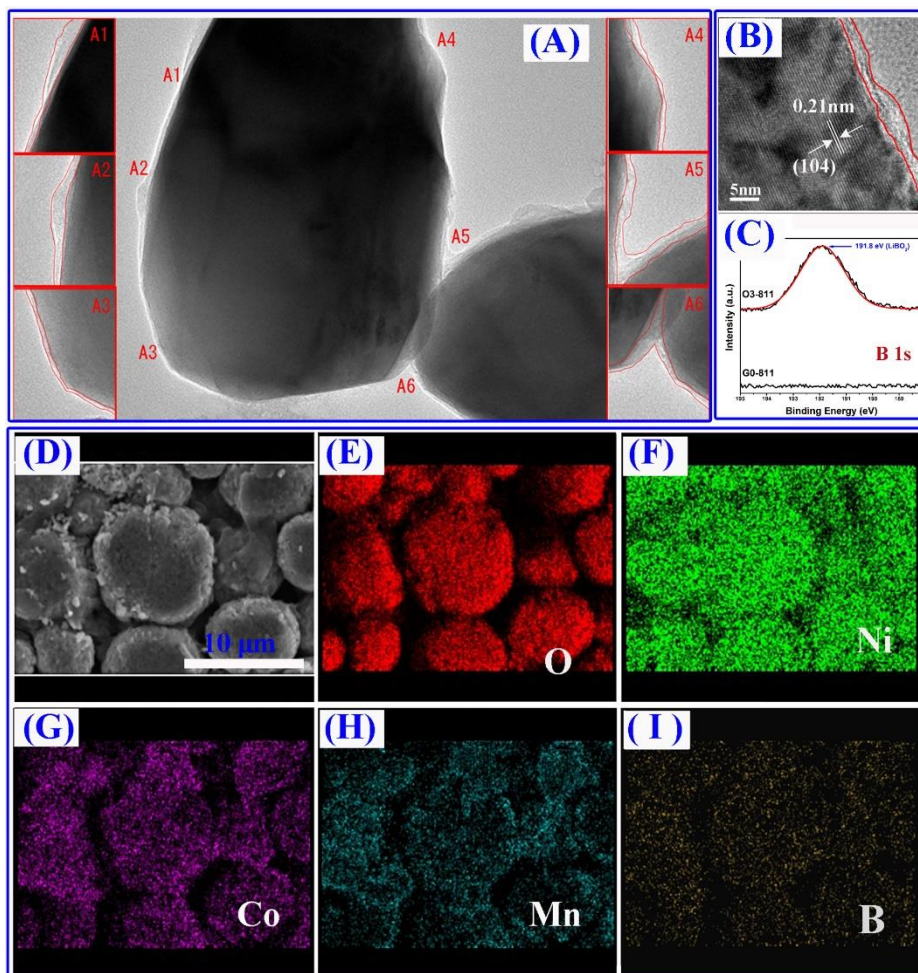


**Figure 3.** (A) TEM image of O3-811, (B) HRTEM image of O3-811, (C) XPS spectra of G0-811 and O3-811 for B1s; EDS mapping images of O3-811: (D) O3-811 sample, (E) O, (F) Ni, (G) Co, (H) Mn, (I) B.

Figure 3 (A) and Figure 3 (B) present TEM and HRTEM images of primary particles of O3-811. Through observation on different areas on primary particles of O3-811 in Figure 3 (A), capsule-like morphology can be seen in which a coating layer with thickness of approximately 3-8 nm is homogeneously deposited onto each primary particle of O3-811. Interplanar distances of 0.21 nm correspond to the (104) crystal planes of NCM with a hexagonal layered crystal structure, which is consistent with the XRD results. To further confirm the introduction of boron, the surface chemical components of G0-811 and O3-811 have been investigated by XPS with representative spectra of B1s

plotted in Figure 3 (C). The uniform dispersion of boron oxide is demonstrated by EDS elemental mapping images, as shown in Figure 3 (D) ~ (I). The peak at binding energy of 191.80 eV can be ascribed to the characteristic peak of  $B^{3+}$  ions in accordance with characteristic peak of B 1S in  $LiBO_2$ , indicating the existence of boron at surface of O3-811, which is in agreement with the results of aforementioned EDS mapping.[25, 26] The elemental mappings of Ni, Co, Mn, O, and B in Figure 3 (D) ~ (I) reveal that these elements are homogeneously distributed in the selected region, which affirms  $LiBO_2$  homogeneously coating on the O3-811 sample.

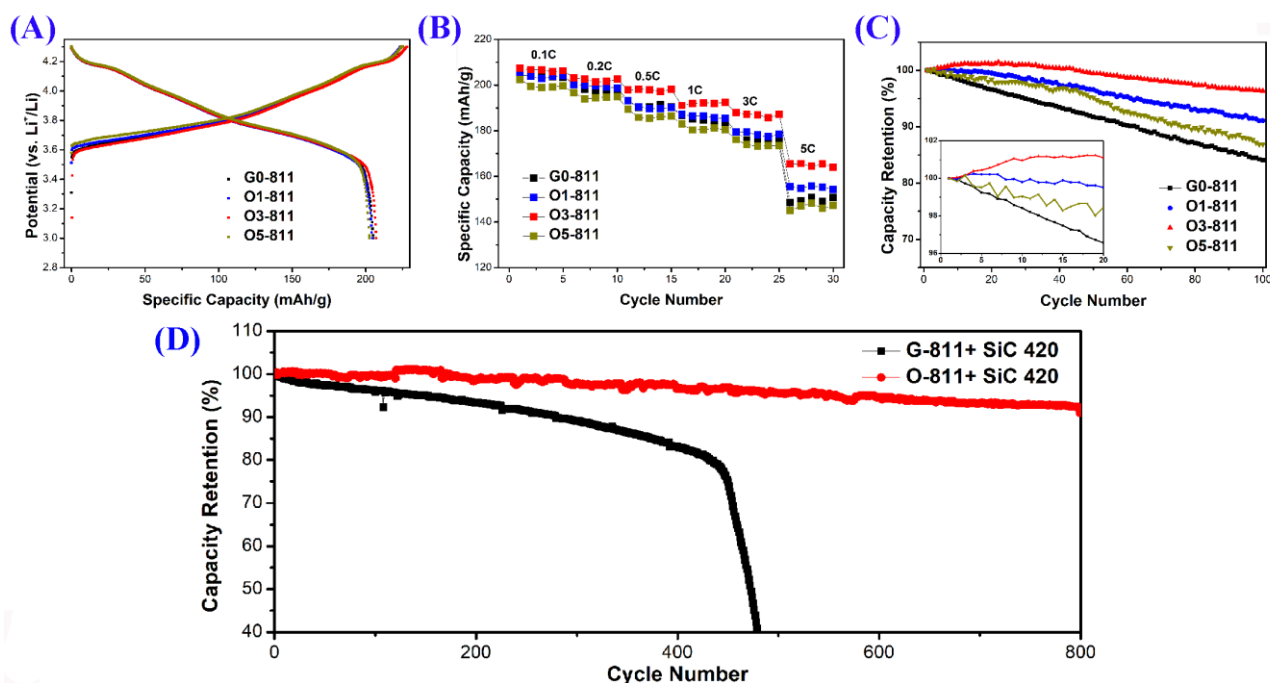


**Figure 4.** Coin-type half-cell test results of G0-811, O1-811, O3-811 and O5-811 between 3.0 and 4.3V (1 C = 200 mA/g): (A) initial charge/discharge profiles at 0.1 C between 3.0 and 4.3 V (1 C = 200 mA/g); (B) rate capability at various current densities, (C) cycling performance at 1 C. (D) Cycling performance of G0-811 and O3-811 tested in pouch-type full cell at 1 C between 2.5 and 4.2 V.

To explore the effect of  $LiBO_2$  encapsulation on NMC811, the electrochemical performances of G0-811 and samples coated with different content of boron were evaluated comparatively using coin type half-cell. Figure 4(A), (B) and (C) display the test results of G0-811, O0-811, O3-811 and O5-811 within the potential range of 3.0–4.3 V vs.  $Li^+/Li$  at room temperature. Figure 4 (A) compares the initial charge-discharge profiles of G0-811, O1-811, O3-811 and O5-811 at a current density of 0.1 C (1C = 200 mA h  $g^{-1}$ ). G0-811 exhibits charge capacity of 224.3 mA h  $g^{-1}$  and discharge capacity 205.1 mA h  $g^{-1}$  at first cycle, indicating that the first cycle efficiency is 91.4%. On the other hand, O3-811 shows 228.2 mA h  $g^{-1}$  and 207.3 mA h  $g^{-1}$ , respectively, which means a first cycle efficiency of 90.8%. The rate capabilities of G0-811, O1-811, O3-811 and O5-811 are presented at various C-rates in Figure 4 (B). The cells are first charged and discharged at 0.1 C for five cycles, followed by cycling at 0.2 C, 0.5 C, 1 C, 2 C, 3 C and 5 C for every five cycles, respectively. The discharge capacities of G0-811, O1-

811, O3-811 and O5-811 decrease with increasing current densities. It can be seen that the O1-811 and O3-811 samples exhibit better rate capabilities than G0-811, especially at higher C-rates. When boron content up to 5000ppm, the discharge capacities of O5-811 at different C-rates are all lower than that of G0-811. So, it is reasonable to conclude that O3-811 is an appropriate design for better electrochemical performances.

The cycle performances of G0-811 and O3-811 have been investigated over 100 cycles at a current density of  $200 \text{ mA g}^{-1}$  between 3.0 and 4.3 V. The results are shown in Figure 4 (C), revealing that the capacity retention for coated samples are all superior to that the unencapsulated sample. G0-811 rapidly declines after 100 cycles with the capacity retention of 84.0%, while the capacity retention of  $\text{LiBO}_2$  encapsulated samples are 91.1% for O1-811, 96.4% for O3-811 and 86.7% for O5-811. It is reasonable to deduce that the superior capacity retention originating from the  $\text{LiBO}_2$  encapsulation treatment, because  $\text{LiBO}_2$  at the surface and interspace effectively suppress electrochemical polarization as well as prevent the bulk from undesired side reaction with the electrolyte.[27,28]

To further evaluate the improved electrochemical performance of  $\text{LiBO}_2$  encapsulated NCM811 under realistic condition, full cells have been tested under 1 C current by using pouch-type G0-811 or O3-811 as cathode material and silicon oxide/graphite composite ( $\text{SiO}_x\text{@C}$ : 420mAh/g) as anode material. As shown in Figure 4(D), O3-811 exhibits superior cycle stability by comparing with G0-811. The pouch cell for O3-811 presents a capacity retention of 91.9% after 800 cycles, while G0-811 displays sever capacity dropping after 430 cycles. Such inspiring improvement in practical use of NCM811 can be ascribed to less electrolyte consuming side reaction and constrained connection loss.[29, 30]

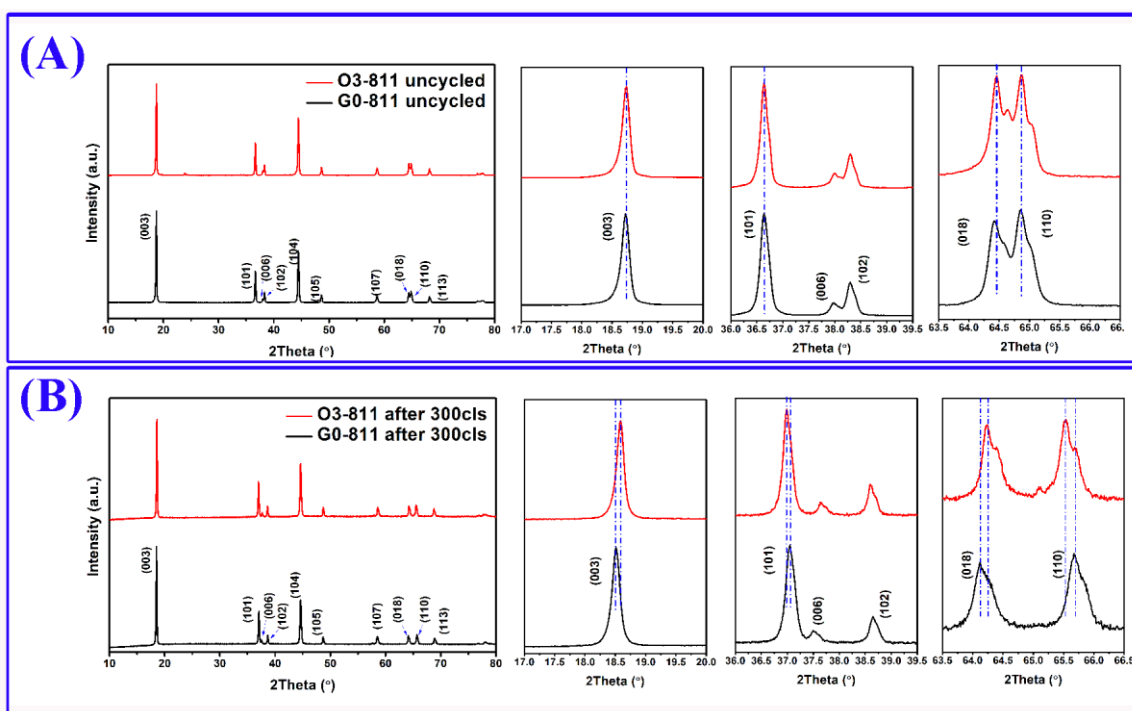


**Figure 5.** XRD patterns and enlarged XRD patterns in selected  $2\theta$  range of G0-811 and O3-811: (A) unencapsulated, (B) after 300 cycles charge-discharge test in a pouch cell.

For understanding on such improvement, the XRD tests for cycled samples are carried out. Figure 5 (A) and (B) show the XRD patterns of uncycled and 300 times charge-discharge cycled materials of G0-811 and O3-811, respectively. For the uncycled samples, there is few differences between the XRD patterns of G0-811 and O3-811. After cycling in a pouch-type full cell for 300 cycles, both G0-811 and O3-811 samples remain well defined layer structure based on a hexagonal  $\alpha$ -NaFeO<sub>2</sub> structure with an  $R\bar{3}m$  space group. As is reported by previous studies, the integrated intensity ratio of  $I_{(003)}/I_{(104)}$  is sensitive to cation mixing, which is often used to testify the degree of  $\text{Li}^+/\text{Ni}^{2+}$  cation mixing in the layered structure.[29, 32, 33] Herein, the integrated intensity ratios of  $I_{(003)}/I_{(104)}$  for G0-811 and O3-811 after 300 cycles in pouch cell are calculated to be 1.26 and 1.53, respectively, suggesting O3-811 remains a much lower degree of cation  $\text{Li}^+/\text{Ni}^{2+}$  mixing than G0-811. Moreover, peak shifts can be observed, which are (003) and (018) towards lower  $2\theta$  degree, while (003) and (110) towards higher  $2\theta$  degree. Such peak shifts indicate a slighter cell expansion in O3-811 than that of G0-811. Additionally, peak broaden and weaken of (006), (102), (018) and (110) are milder in O3-811 than in G-811, signifying a less severity of irreversible cell expansion and contraction in O3-811 than G0-811 during charge-discharge cycles.[32, 33]

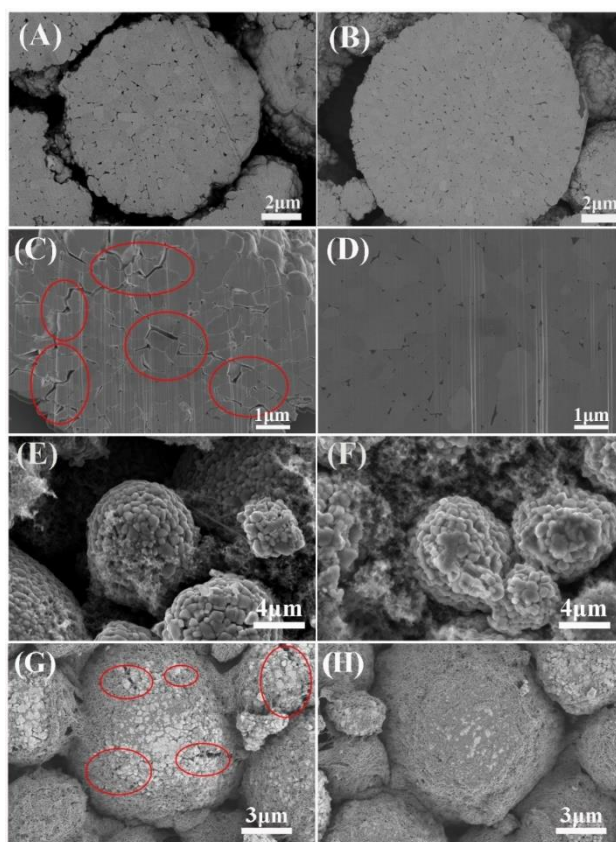


**Figure 6** FIB-SEM images on the cross-section of uncycled G0-811(A) and O3-811 (B); FIB-SEM images on the cross-section of G0-811(C) and O3-811 (D) after 100 cycles in coin cells; SEM images of uncycled G0-811(E) and O3-811 (F); SEM images of G0-811(G) and O3-811 (H) after 300 cycles in pouch cells.

FIB-SEM images on the cross-section of G0-811 and O3-811 powder without cycling are displayed in Figure 6(A) and (B), respectively. Both G0-811 and O3-811 secondary spheres are comprised of long primary particles with 300-700nm. However, O3-811 shows a relatively closer packed structure, in which the void between primary particle is much less than that of G0-811. To further understand the degradation of NCM811, FIB-SEM images on the cross-section are collected on cycled electrode of G0-811 and O3-811 in Figure 6 (C) and (D), respectively. Compared with G0-811 before cycling in Figure 6 (A), there appears apparent internal microcracking in cycled G0-811 in Figure 6 (C). Such cracks lead to direct contact of the internal crystal grains to the erosive electrolyte, causing electrochemical performance to deteriorate drastically.

However, the cracking of the secondary particles is greatly restrained for O3-811 after 100 cycles as displayed in Figure 6 (D). Such results are also certified by the SEM images of G0-811 and O3-811 electrodes after 300 cycles in pouch cells in Figure 6 (E) and (F), respectively. The large-scale intergranular cracking can be easily observed in the cycled G0-811 in Figure 6 (G), but hardly found in the O3-811 in Figure 6 (H). Such improvement is mainly attributed to boron oxide coating on surface of the O3-811 primary particles. The intragranular coating layer inhibits the unwanted exposure of O3-811 particles to the electrolyte, preventing the cathode electrode from forming structure decay and transitional elements dissolution. Moreover, such coating strategy promotes strengthening of mutual-combination of primary particles so that disconnection is significantly suppressed.[31-34] Therefore, thus modified NCM811 shows promising electrochemical performances.

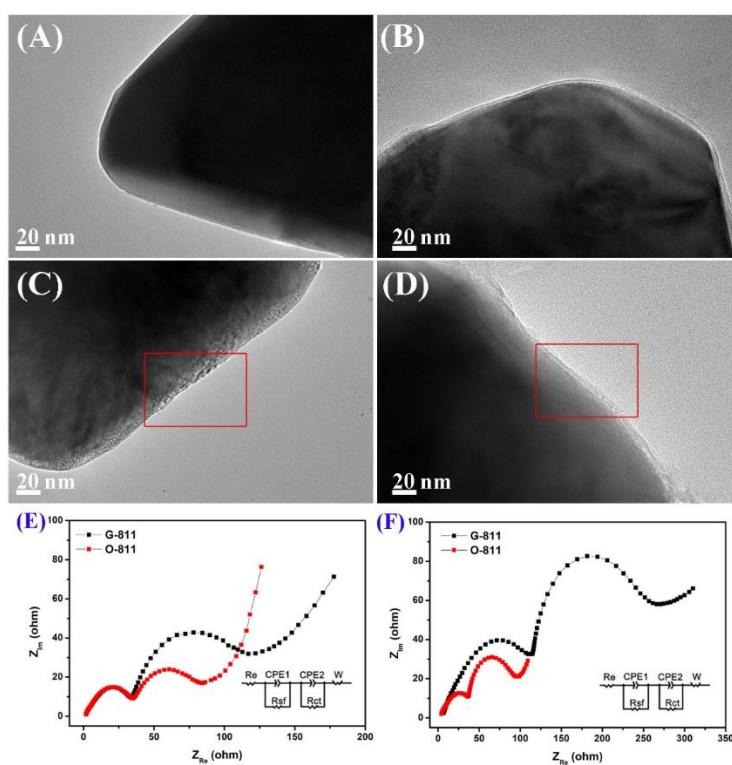


**Figure 7** TEM images of (A) G0-811 before cycled, (B) O3-811 before cycled, (C) G0-811 after 60 cycles in the coin cell, (D) O3-811 after 60 cycles in the coin cell. EIS for as prepared G0-811 and O3-811 of (E) after 5 charge/discharge cycles, (F) after 60 cycles, the equivalent circuit within the insets are attached to both images.

The primary particle of G-811 and O-811 at 5<sup>th</sup> cycles in coin cells are observed by TEM, and corresponding images are displayed in Figure 7 (A) and (B), respectively. G0-811 has a smooth and bald surface without any coating layer or corrosion region, while O3-811 is encapsulated by coating layer of LiBO<sub>2</sub> with thickness around 3-10 nm. Furthermore, the primary particle of G0-811 and O3-811 after 60 cycles in coin cells are observed and displayed in Figure 7 (C) and (D), respectively. The surface of G0-811 becomes obviously eroded originating from side reaction between G0-811 and electrolyte. Nevertheless, the primary particle of O3-811 remains clean and smooth, indicating those unwanted side reactions and surface invasions are successfully suppressed by LiBO<sub>2</sub> encapsulation.[29, 30, 35-37]

To track the degradation along cycling of G0-811 and O3-811 as cathode materials in the coin cell, Electrochemical impedance spectroscopy (EIS) is employed. Figure 7 (E) and (F) display the Nyquist plot for G0-811 and O3-811 at the 5<sup>th</sup> and 60<sup>th</sup> cycles, respectively. Each Nyquist curve in the EIS plots is comprised of three parts: 1) the semicircle in the high-frequency region referring to  $R_{sf}$  associated with surface film impedance; 2) the second semicircle in the medium-frequency range referring to  $R_{ct}$  that represents the charge transfer impedance; 3) An oblique line in the low frequency region which is considered as the Warburg impedance ( $W_o$ ).[38]

According to the fitted results in Table S2, the value of  $R_e$  and  $R_{sf}$  for G0-811 and O3-811 cells are similar after 5 cycles. However, the  $R_{ct}$  value for G0-811 is much larger than that of O3-811, which is probably attributed to the closer packed structure with intimate coated surface of O3-811.[39-41] Moreover, the situation changed dramatically after 60 cycles on G0-811 and O3-811 are carried out. The value of  $R_e$ ,  $R_{sf}$  and  $R_{ct}$  for O3-811 stays steady with little augment. While for the O3-811 electrode,  $R_e$ ,  $R_{sf}$  and  $R_{ct}$  reveal huge increase. It has been reported that Ni-rich cathode material suffers an irreversible microstructure degradation as well as peeling off the current collector, which cause not only the rise of the internal resistance and the fresh deposition of SEI, but also the increase of charge transfer resistance.[42] Here by comparing O3-811 with G0-811, the intergranular coating of boron oxide is possible to suppress and alleviate the degradation of Ni-rich cathode material.

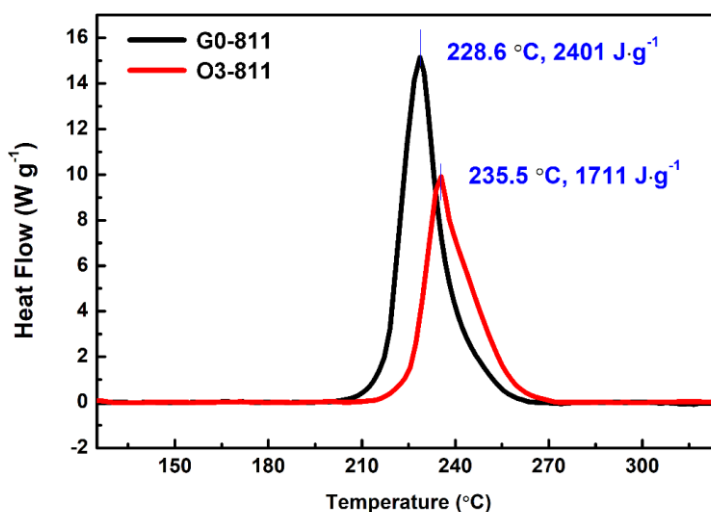


**Figure 8.** DSC curves of G0-811 and O3-811 at the state of charge of 4.3 V.

DSC is used to evaluate the thermal stability of the cathode materials after 3 cycles of charge-discharge and then charged the SOC of 4.3 V full charged. As shown in Figure 8, G0-811 shows an exothermic peak at 228.6 °C with an overall heat generation of 2401 J·g<sup>-1</sup>, whereas O3-811 exhibits a higher exothermic peak temperature at 235.5°C with an overall heat generation of 1711 J·g<sup>-1</sup>. The result significantly prove that the encapsulation NCM811 with LiBO<sub>2</sub> on both secondary spheres and primary particles benefits the thermal stability of Ni-rich cathode material. Thus, the obtained coating structure effectively protects the surface of the NCM811 from attack of acid like HF.[43,44] The capsule-like structure retards the electrolyte consuming side reaction and phase transition reaction in the active NCM811 bulk material.

#### 4. CONCLUSION

In this work, different amount of LiBO<sub>2</sub> encapsulated LiNi<sub>0.8</sub>Co<sub>0.1</sub>Mn<sub>0.1</sub>O<sub>2</sub> were obtained through a two-steps process. Among thus treated samples, O3-811 shows the best electrochemical performances. And it exhibits greatly alleviated cycle deterioration and particle cracking than G0-811. It is demonstrated that the improvement of cycle performance and thermal stability of NCM811 can be ascribed to the following factors: 1) strengthening the connection of primary particles; 2) reducing the phase transition reaction and over expansion of cell; 3) suppressing the unwanted electrolyte corrosion reaction. The strategy of encapsulating NCM811 into LiBO<sub>2</sub> is proved to be of effectiveness in 294 Wh/kg pouch cell system, which can be further applied into commercial use of Ni-rich cathode material for higher energy density lithium ion batteries.

#### ACKNOWLEDGEMENTS

The authors would like to acknowledge the National Natural Science Foundation of China (51971250), the National Key Research and Development Program of China (Grant No. 2018YFB010400), the State Key Laboratory of Powder Metallurgy at Central South University.

#### SUPPORTING INFORMATION

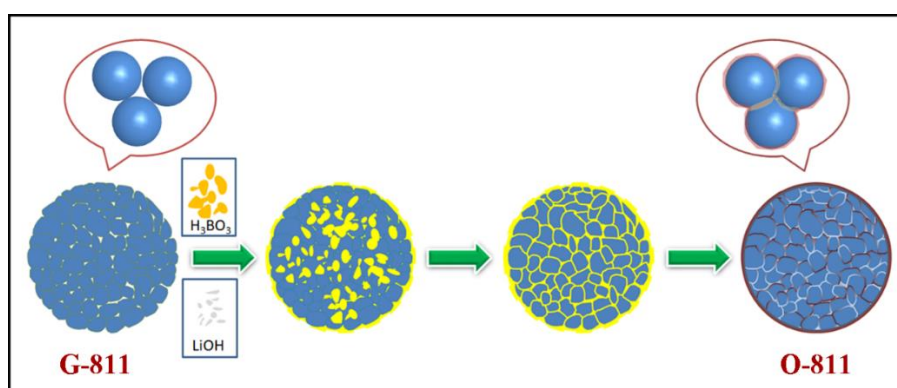


**Figure S1.** Schematic illustration for the preparation of O1-811, O3-811 and O5-811) by boron oxides encapsulation on both second spheres and primary particles

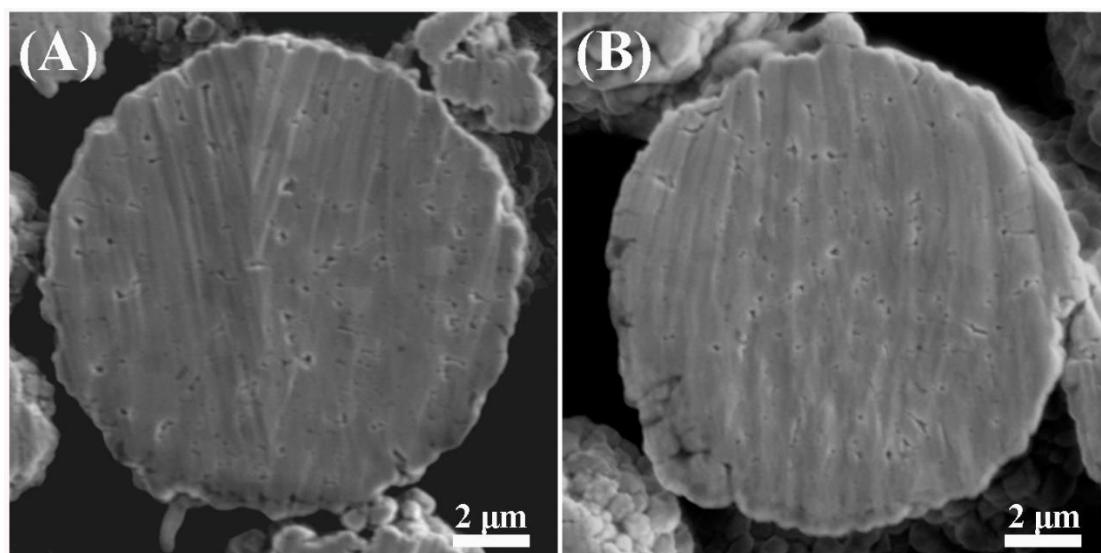


**Figure S2.** FIB-SEM images on the cross-section (A) G0-811 and (B) O3-811

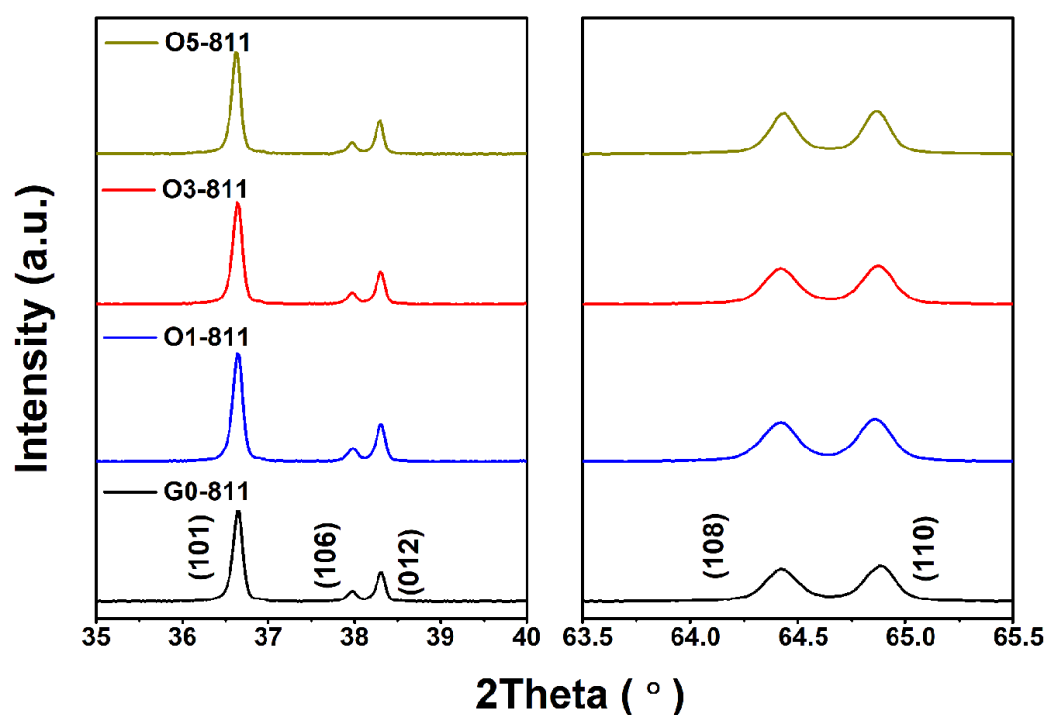


**Figure S3.** the XRD patterns for NCM811 samples.

**Table S1.** The content of Ni/Co/Mn/B in G0-811, O1-811, O3-811 and O5-811.

sample	Ni	Co	Mn	B
		%		ppm
G0-811	47.29	5.94	5.54	\
O1-811	47.36	5.95	5.48	984
O3-811	47.33	5.94	5.52	2972
O5-811	47.35	5.97	5.53	4899

**Table S2.** Fitted results of the EIS for G0-811 and O-S811 at 100% SOC of 5 cycles and 100 cycles.

<b>100%SOC@5cycles</b>	<b>R<sub>e</sub> (Ω)</b>	<b>R<sub>sf</sub> (Ω)</b>	<b>R<sub>ct</sub> (Ω)</b>
<b>G0-811</b>	2.1	43.4	110.6
<b>O3-811</b>	2.7	46.9	68.8
<b>100%SOC @60cycles</b>	<b>R<sub>e</sub> (Ω)</b>	<b>R<sub>sf</sub> (Ω)</b>	<b>R<sub>ct</sub> (Ω)</b>
<b>G0-811</b>	7.2	154.2	207.4
<b>O3-811</b>	3.6	52.8	78.1

## References

1. J. Kim, H. Lee, H. Cha, M. Yoon, M. Park and J. Cho, *Adv. Energy Mater.*, 8(2018) 1702028.
2. N. Nitta, F. Wu, J. T. Lee and G. Yushin, *Mater. Today*, 18(2015) 252-264.
3. W. Liu, P. Oh, X. Liu, M.-J. Lee, W. Cho, S. Chae, Y. Kim and J. Cho, *Angew. Chem. Int. Edit.*, 54(2015) 4440-4457.
4. A. O. Kondrakov, H. Geßwein, K. Galdina, L. de Biasi, V. Meded, E. O. Filatova, G. Schumacher, W. Wenzel, P. Hartmann, T. Brezesinski and J. Janek, *J. Phys. Chem. C*, 121(2017) 24381-24388.
5. J. Zhu and G. Chen, *J. Mater. Chem. A*, 7(2019) 5463-5474.
6. J.-M. Lim, T. Hwang, D. Kim, M.-S. Park, K. Cho and M. Cho, *Sci. Rep.*, 7(2017) 39669.
7. L. Mu, R. Lin, R. Xu, L. Han, S. Xia, D. Sokaras, J. D. Steiner, T.-C. Weng, D. Nordlund, M. M. Doeff, Y. Liu, K. Zhao, H. L. Xin and F. Lin, *Nano Lett.*, 18(2018) 3241-3249.
8. K. Min and E. Cho, *Phys. Chem. Chem. Phys.*, 20(2018) 27115-27124.
9. D.-S. Ko, J.-H. Park, S. Park, Y. N. Ham, S. J. Ahn, J.-H. Park, H. N. Han, E. Lee, W. S. Jeon and C. Jung, *Nano Energy*, 56(2019) 434-442.
10. S.-H. Lee, B.-S. Jin and H.-S. Kim, *Sci. Rep.*, 9(2019), 17541.
11. G. Hu, M. Zhang, L. Wu, Z. Peng, K. Du and Y. Cao, *ACS Appl. Mater. Interfaces*, 8(2016) 33546-33552.
12. S. Neudeck, F. Strauss, G. Garcia, H. Wolf, J. Janek, P. Hartmann and T. Brezesinski, *Chem. Commun.*, 55(2019) 2174-2177.
13. L. Li, M. Xu, Q. Yao, Z. Chen, L. Song, Z. Zhang, C. Gao, P. Wang, Z. Yu and Y. Lai, *ACS Appl. Mater. Interfaces*, 8(2016) 30879-30889.
14. S. H. Jang, K.-J. Lee, J. Mun, Y.-K. Han and T. Yim, *J. Power Sources*, 410-411(2019) 15-24.
15. K. Du, H. Xie, G. Hu, Z. Peng, Y. Cao and F. Yu, *ACS Appl. Mater. Interfaces*, 8(2016) 17713-17720.
16. B. Han, B. Key, S. H. Lapidus, J. C. Garcia, H. Iddir, J. T. Vaughey and F. Dogan, *ACS Appl. Mater. Interfaces*, 9(2017) 41291-41302.
17. Y. Xia, J. Zheng, C. Wang and M. Gu, *Nano Energy*, 49(2018) 434-452.
18. I. D. Campbell, K. Gopalakrishnan, M. Marinescu, M. Torchio, G. J. Offer and D. Raimondo, *J. Energy Storage*, 22(2019) 228-238.
19. J.-H. Kim, K.-J. Park, S. J. Kim, C. S. Yoon and Y.-K. Sun, *J. Mater. Chem. A*, 7(2019) 2694-2701.
20. B. Han, S. Xu, S. Zhao, G. Lin, Y. Feng, L. Chen, D. G. Ivey, P. Wang and W. Wei, *ACS Appl. Mater. Interfaces*, 10(2018) 39599-39607.
21. M. Liu, N. Liu, J. Tan, Y. Su, W. Deng, L. Chen, R. Xue and Q. Zhang, *ChemElectroChem*, 6(2019) 3057-3064.
22. B. V. R. Chowdari and Z. Rong, *Solid State Ionics*, 90, (1996) 151-160.

23. R. Ma, Z. Zhao, J. Fu, H. Lv, C. Li, B. Wu, D. Mu and F. Wu, *ChemElectroChem*, 7(2020) 2637-2642.
24. T. He, Y. Lu, Y. Su, L. Bao, J. Tan, L. Chen, Q. Zhang, W. Li, S. Chen and F. Wu, *ChemSusChem*, 11(2018) 1639-1648.
25. W. Liu, X. Li, D. Xiong, Y. Hao, J. Li, H. Kou, B. Yan, D. Li, S. Lu, A. Koo, K. Adair and X. Sun, *Nano Energy*, 44(2018) 111-120.
26. W. Hu, C. Zhang, H. Jiang, M. Zheng, Q.-H. Wu and Q. Dong, *Electrochim. Acta*, 243(2017) 105-111.
27. Y. Ding, R. Wang, L. Wang, K. Cheng, Z. Zhao, D. Mu and B. Wu, *Energy Procedia*, 105(2017) 2941-2952.
28. J. Zhang, H. Zhong, C. Zheng, Y. Xia, C. Liang, H. Huang, Y. Gan, X. Tao and W. Zhang, *J. Power Sources*, 391(2018) 73-79.
29. W. Zhang, L. Liang, F. Zhao, Y. Liu, L. Hou and C. Yuan, *Electrochim. Acta*, 340(2020) 135871.
30. F. Friedrich, B. Strehle, A. T. S. Freiberg, K. Kleiner, S. J. Day, C. Erk, M. Piana and H. A. Gasteiger, *J. Electrochem. Soc.*, 166(2019) A3760-A3774.
31. K. Park, J.-H. Park, S.-G. Hong, B. Choi, S. Heo, S.-W. Seo, K. Min and J.-H. Park, *Sci. Rep.*, 7(2017) 44557.
32. B. Zhang, P. Dong, H. Tong, Y. Yao, J. Zheng, W. Yu, J. Zhang and D. Chu, *J. Alloy Compd.*, 706(2017) 198-204.
33. D. Mohanty, K. Dahlberg, D. M. King, L. A. David, A. S. Sefat, D. L. Wood, C. Daniel, S. Dhar, V. Mahajan and M. Lee, *Sci. Rep.*, 6(2016) 26532.
34. H. Yu, S. Qian, L. Yan, P. Li, X. Lin, M. Luo, N. Long, M. Shui and J. Shu, *J. Alloy Compd.*, 667(2016) 58-64.
35. Q. Wang, C.-H. Shen, S.-Y. Shen, Y.-F. Xu, C.-G. Shi, L. Huang, J.-T. Li and S.-G. Sun, *ACS Appl. Mater. Interfaces*, 9(2017) 24731-24742.
36. H. Liu, M. Wolf, K. Karki, Y.-S. Yu, E. A. Stach, J. Cabana, K. W. Chapman and P. J. Chupas, *Nano Lett.*, 17(2017) 3452-3457.
37. A. O. Kondrakov, A. Schmidt, J. Xu, H. Geßwein, R. Mönig, P. Hartmann, H. Sommer, T. Brezesinski and J. Janek, *J. Phys. Chem. C.*, 121 (2017) 3286-3294.
38. P. Xiao, T. Lv, X. Chen and C. Chang, *Sci. Rep.*, 7(2017) 1408.
39. M. Dong, Z. Wang, H. Li, H. Guo, X. Li, K. Shih and J. Wang, *Acs Sustain. Chem. Eng.*, 5, (2017) 10199-10205.
40. J. Fang, Y. Xu, G. Xu, S. Shen, J. Li, L. Huang and S. Sun, *J. Power Sources*, 304(2016) 15-23.
41. Y.-K. Sun, Z. Chen, H.-J. Noh, D.-J. Lee, H.-G. Jung, Y. Ren, S. Wang, C. S. Yoon, S.-T. Myung and K. Amine, *Nat. Mater.*, 11(2012) 942-947.
42. Z. Li, F. Du, X. Bie, D. Zhang, Y. Cai, X. Cui, C. Wang, G. Chen and Y. Wei, *J. Phys. Chem. C*, 114(2010) 22751-22757.
43. X. Liu, D. Ren, H. Hsu, X. Feng, G.-L. Xu, M. Zhuang, H. Gao, L. Lu, X. Han, Z. Chu, J. Li, X. He, K. Amine and M. Ouyang, *Joule*, 2(2018) 2047-2064.
44. R. Zhang, Y. Wang, X. Song, G. Li, S. Liu and X. Gao, *ChemElectroChem*, 7(2020) 2042-2047.